APPLIED SCIENCES AND ENGINEERING

Phase-change metal ink with pH-controlled chemical sintering for versatile and scalable fabrication of variable stiffness electronics

Simok Lee[1]†, Gun-Hee Lee[2,3]†, Inho Kang[1], Woojin Jeon[2], Semin Kim[4], Yejin Ahn[1], Choong Yeon Kim[1,5], Do A Kwon[6,7], Michael D. Dickey[8], Steve Park[9,10]*, Seongjun Park[2,11,12,13,14]*, Jae-Woong Jeong[1,4,10,15]*

Variable stiffness electronics represent the forefront of adaptive technology, integrating rigid and soft electronics in a single system through dynamic mechanical modulation. While gallium's high modulus tuning ratio and rapid phase transitions make it ideal for transformative electronic systems (TES), its liquid-state instability, high surface tension, and unintended phase transitions during processing pose substantial challenges. Here, we introduce STiffness-Adjustable temperature-Responsive ink (STAR ink), a chemically sinterable gallium composite electronic ink designed to overcome these obstacles. STAR ink enables high-resolution (~50 micrometers) circuit patterning, large-scale batch fabrication, and three-dimensional structure coating at room temperature. Through pH-controlled chemical sintering, STAR ink–based TES exhibits exceptional mechanical tunability (tuning ratio: 1465) and electrical conductivity (2.27×10^6 siemens per meter). Demonstrated applications—from multilayered variable stiffness printed circuit boards (PCBs) matching standard PCBs' complexity to body-temperature responsive neural probe—underscore STAR ink's potential for reconfigurable electronics across consumer electronics and biomedical devices.

INTRODUCTION

The evolution of modern electronics is driven by advancements in materials, which determine the function and structure of devices. For example, the advent of high-performance semiconductors and the use of high-conductivity metals have marked a pivotal breakthrough, enabling high-performance integrated electronics (*1*–*4*). However, the inherent rigidity of these materials limits their use in applications requiring flexibility and stretchability, such as conforming to human body contours or adapting to various three-dimensional (3D) structures. To address this, researchers have explored a new class of materials—soft electronic materials (*5*–*12*). These materials combine elastomers with nano- and microscale conductive materials (*5*, *6*, *13*), fostering the development of flexible and stretchable electronics that introduce unprecedented form factors. Consequently, rigid electronics thrive in applications that require stable solid interfaces, such as smartphones and laptops, while flexible and stretchable technologies excel in wearable and implantable devices that adapt to body movements (*14*, *15*). Despite their differences, modern electronics all share a common trait: meticulous design to optimize specific purposes, which has been the guiding principle in the development of advanced electronics.

As technology advances and user demands evolve, however, the need for electronic devices that can serve multiple functions across various scenarios has become increasingly apparent (*16*–*19*). While both rigid and flexible/stretchable electronics excel in their designated roles, their fixed form factors limit adaptability and broader utility, often necessitating the development and use of multiple specialized devices (*20*–*22*). Recently, efforts have aimed to frontier in electronics by developing devices that can dynamically alter their shape and mechanical properties to adapt to desired applications. These electronics, referred to as transformative electronic systems (TES), enable a single device to serve multiple purposes across various applications through a seamless transition between rigid and adaptive soft forms (*23*–*34*).

The key to developing TES lies in selecting materials with excellent stiffness-tuning capabilities. Various stimuli-responsive materials, including hydrogel (*35*–*37*), magneto-/electroresponsive polymers (*38*, *39*), and shape memory polymers (*40*–*42*), have been actively explored for the purpose. However, these materials face performance limitations due to low modulus tuning ratio (*42*, *43*) and low power efficiency (*44*, *45*). In addition, because these materials are not inherently conductive, they cannot form electronics by themselves, needing the integration of a separate circuit layer to enable electronics functionality within a stiffness-tunable framework (*37*, *40*, *42*, *43*). This multilayer structure not only complicates the fabrication process of TES but also results in bulky end products.

Gallium emerges as a promising candidate for applications involving biological interfacing due to its combination of properties.

---

[1]School of Electrical Engineering, Korea Advanced Institute of Science and Technology (KAIST), 291 Daehak-ro, Yuseong-gu, Daejeon 34141, Republic of Korea. [2]Medical Research Center, Seoul National University, Seoul 03080, Republic of Korea. [3]Departments of Cogno-Mechatronics Engineering and Optics and Mechatronics Engineering, Pusan National University, Busan 46241, Republic of Korea. [4]Graduate School of Semiconductor Technology, Korea Advanced Institute of Science and Technology (KAIST), 291 Daehak-ro, Yuseong-gu, Daejeon 34141, Republic of Korea. [5]KAIST Information and Electronics Research Institute, Daejeon 34141, Republic of Korea. [6]Research Laboratory of Electronics, Massachusetts Institute of Technology (MIT), Cambridge, MA 02139, USA. [7]Department of Mechanical Engineering, Massachusetts Institute of Technology (MIT), Cambridge, MA 02139, USA. [8]Department of Chemical and Biomolecular Engineering, North Carolina State University (NCSU), Raleigh, NC 27606, USA. [9]Department of Materials Science and Engineering, Korea Advanced Institute of Science and Technology (KAIST), 291 Daehak-ro, Yuseong-gu, Daejeon 34141, Republic of Korea. [10]KAIST Institute for NanoCentury, Daejeon 34141, Republic of Korea. [11]Department of Biomedical Sciences, College of Medicine, Seoul National University, Seoul 03080, Republic of Korea. [12]School of Transdisciplinary Innovations, Seoul National University, Seoul 03080, Republic of Korea. [13]Interdisciplinary Program in Bioengineering, College of Engineering, Seoul National University, Seoul 08826, Republic of Korea. [14]Department of Transdisciplinary Medicine, Seoul National University Hospital, Seoul 03080, Republic of Korea. [15]KAIST Institute for Health Science and Technology, Daejeon 34141, Republic of Korea.
*Corresponding author. Email: jjeong1@kaist.ac.kr (J.-W.J.); seongjunpark@snu.ac.kr (Se.P.); stevepark@kaist.ac.kr (St.P.)
†These authors contributed equally to this work.

Its elastic modulus tuning property ($E \sim 0$ Pa at its liquid state and $E \sim 9.8$ GPa in its solid state) allows for marked mechanical transformation. This capability is enhanced by its phase transition occurring near body temperature (above 30°C) (*34*, *46*, *47*), a distinctive feature among low–melting-point metals (*30*, *48*, *49*). In addition, gallium's high electrical conductivity (3.4×10^6 S m^{-1}) (*50*) makes it suitable for creating dual-functional transformative circuits that integrate electrical and mechanical functionalities, eliminating the need for a separate mechanically tunable framework, thereby facilitating the development of compact, high-performance TES. Despite these attractive characteristics, gallium has critical drawbacks, such as fluidic instability, high surface tension (*51*), and unwanted phase transitions during processing, which inhibit high-resolution patterning and robust integration with integrated circuit chips and surface-mounted devices (SMDs). These issues have limited gallium's full potential and restricted its use to mechanical frameworks within TES (*31*, *33*, *34*). Recent research has partially addressed one of these challenges—the high surface tension issue—by mixing liquid metal with copper (*28*). The modified rheology of this ink allows patterning the circuit; however, this ink can cause nozzle clogging during direct ink writing (DIW) due to unwanted solidification at room temperature. To prevent this, the ink must be maintained above gallium's melting temperature (29.8°C), which complicates fabrication under ambient conditions. In addition, the gradual formation of copper-gallium intermetallic phases ($CuGa_2$) over time can degrade the ink's mechanical tunability (*52*). Furthermore, the current process is limited to nozzle-based printing, restricting its broader applicability across diverse fabrication techniques.

In this study, we introduce a room temperature processable, gallium-based STiffness-Adjustable temperature-Responsive electronic ink (STAR ink) that overcomes ongoing limitations of pristine gallium and the previous gallium-copper composite ink (*28*) in facile manufacturing of intricate TES (Fig. 1A and table S1). STAR ink is produced by dispersing micro-sized gallium particles within a hydrophilic polyurethane (HPU) template dissolved in dimethyl sulfoxide (DMSO). The initial neutral pH (*7*) of DMSO ensures the formation of well-dispersed, homogeneous ink with optimized rheological properties (e.g., high viscosity and low surface tension), enabling high-resolution printing. Upon heating, DMSO decomposes and creates acidic conditions (pH 5.5), which sinters the dispersed gallium particles and interconnects them within the HPU matrix. This pH-controlled chemical sintering represents a key solution that uniquely addresses gallium's limitations. By separating dispersion and sintering stages through pH control, we achieve optimal rheology for printing under neutral conditions and then create conductive pathways through oxide removal under acidic conditions. This prevents unwanted solidification during processing while enabling stable gallium particle interconnection postprinting, a capability not achieved in previous gallium-based systems. These factors collectively enable high-resolution (~50 μm) and multilayer printing with excellent process stability, establishing transformative electronic circuits with complexity comparable to standard printed circuit boards (PCBs). STAR ink facilitates large-scale and batch fabrication of TES, customized circuit patterning, and coating on complex 3D structures, all of which are achievable through a room temperature solution process compatible with various fabrication methods such as screen printing (*53*, *54*) and dip coating (*55*). TES fabricated with STAR ink, referred to as "STAR TES," exhibits high electrical conductivity (2.27×10^6 S m^{-1}), high stiffness tunability (bending stiffness tuning ratio of ~1500 for a 600-μm-thick device), and rapid bidirectional rigid-soft mode conversion.

On the basis of these features, we demonstrate multifunctional STAR TES for wearable and implantable applications, showcasing unprecedented mechanical and electrical properties. One application is a multilayered high-density transformative PCB (T-PCB) with ~50-μm linewidth, capable of converting between rigid portable electronics and flexible wearable health care devices. Another application showcases an injectable multifunctional neural probe that softens upon brain insertion, offering easy handling and implantation during surgery in rigid mode and high biomechanical compatibility with brain tissue in soft mode postimplantation. These applications underscore the practical utility and high versatility of STAR ink across various fields and highlight its potential to drive the development of advanced, adaptive electronic systems, propelling the field of transformative electronics forward.

RESULTS

Overview of chemically sintered STAR ink and its versatile solution process for TES

The key advantage of STAR ink lies in its ability to enable high-resolution, stable printing in the solution state, followed by a post–chemical sintering process that brings in electrical conductivity and phase transition capabilities to the resulting TES. STAR ink, composed of micro-sized gallium particles (~8 μm) dispersed within an HPU-DMSO solution, effectively overcomes the inherent high surface tension and fluidic instability of bare gallium (fig. S1). By enhancing wettability and preventing unwanted phase transitions during printing, STAR ink enables high-resolution patterning (minimum feature size: 50 μm) and improves process stability. Upon curing, the gallium particles chemically sinter within the HPU template, forming a conductive network that guarantees both electrical conductivity and phase transition capabilities in a TES. Figure 1B demonstrates that STAR ink enables reliable high-resolution, large-area patterning of TES and its 193-fold change in Young's modulus between its soft and rigid modes (soft mode: 552.3 kPa and rigid mode: 106.7 MPa).

Figure 1 (C to F) illustrates the fundamental characteristics of STAR ink, highlighting its high-resolution patternability with multilayer integration, large-scale and batch fabrication, conforming coating on complex 3D structures, and high electrical conductivity in both soft and rigid modes. The high-resolution and multilayered patternability of STAR ink enables intricate and sophisticated TES designs (Fig. 1C), comparable to the complexity of standard PCBs. This is achieved through the solution-state STAR ink's compatibility with various printing and coating methods. Techniques such as screen printing facilitate customizable patterning over large areas and mass fabrication of TES (Fig. 1D and fig. S2), while dip coating supports conformal coating on complex 3D structures (Fig. 1E). The fabricated STAR TES exhibits stable and high electrical conductivity in both soft and rigid modes, along with excellent mechanical tunability (Fig. 1F). This feature eliminates the need for a separate stiffness-tuning platform required by previous transformative devices (*30*, *34*), thereby simplifying TES design and fabrication.

Overall, the development of STAR ink and its solution process addresses the limitations of pristine gallium, making a notable advancement in TES manufacturing. This innovative approach enables the fabrication of highly adaptive, multifunctional devices with exceptional

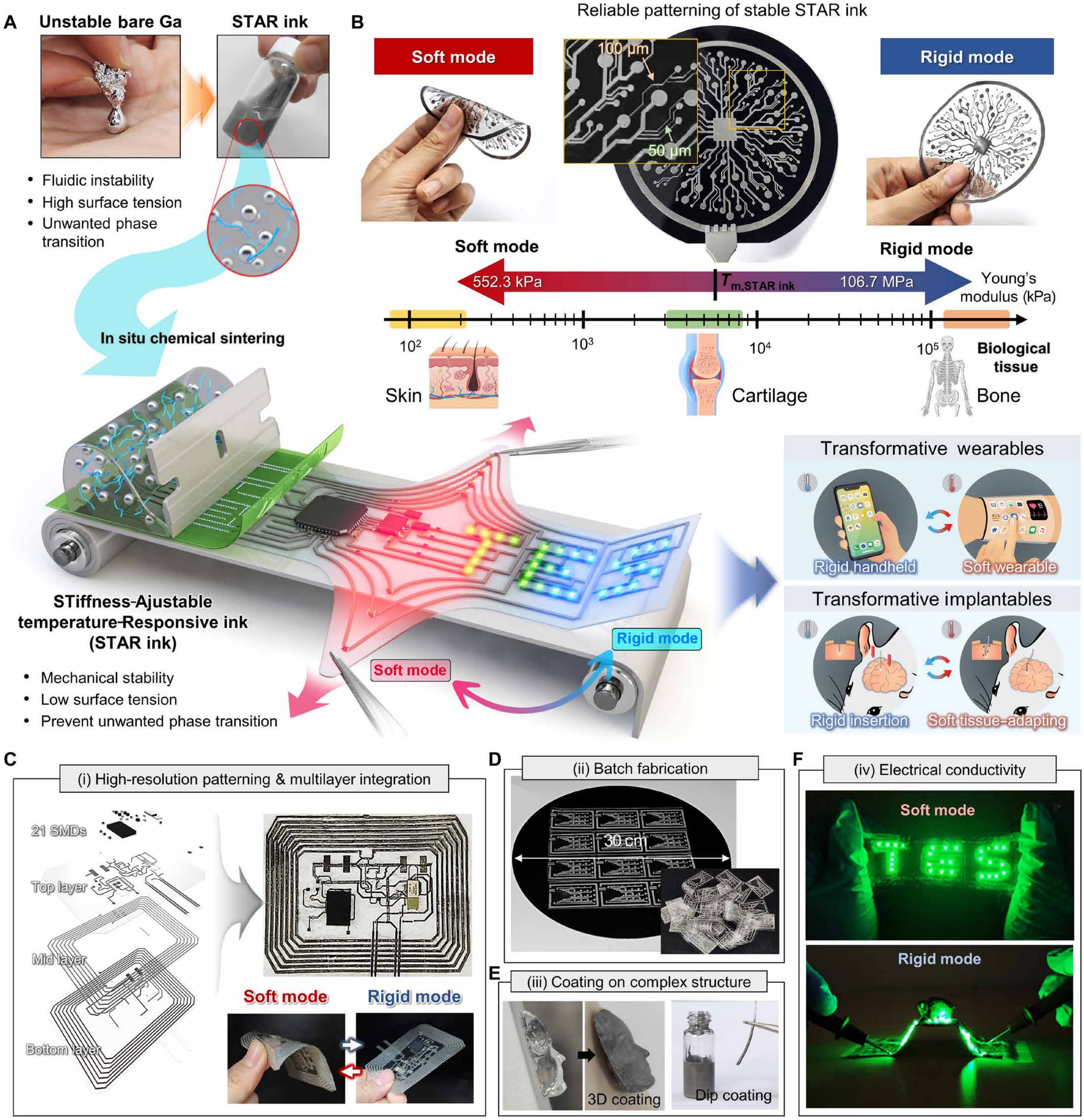

Fig. 1. STAR electronic ink for versatile fabrication of TES via a solution process at room temperature. (**A**) Schematic illustration of the room temperature solution process of STAR ink for fabrication of mechanically transformative electronics. (**B**) Photograph highlighting the large-area patternability of STAR ink for TES, demonstrating its mechanical convertibility between the tissue-like soft mode and the bone-like rigid mode, achieving a 193-fold difference in Young's modulus. (**C** to **F**) Key features of STAR ink: (C) High-resolution patternability with multilayer integration, allowing design complexity comparable to the standard PCB, (D) batch fabrication capability, (E) outstanding coatability on various 3D structures, and (F) excellent electrical conductivity in both soft and rigid modes.

stiffness tunability and high-resolution patterning capabilities comparable to standard photolithography.

Materials and characteristics of STAR ink

Reliable and consistent solution-state STAR ink can be achieved by blending HPU, DMSO, and gallium particles. Initially, HPU was dissolved in DMSO, and then gallium was introduced into the solution through tip sonication, dispersing the gallium particles (fig. S3). Our pH-controlled chemical sintering strategically manipulates pH conditions at different stages of the fabrication process. Initially, the neutral pH (7) of DMSO promotes stable dispersion of gallium particles. In addition, as a polar organic solvent, DMSO effectively dissolves HPU, enabling homogeneous mixing of the gallium particles within the polymer matrix. The viscosity of the STAR ink can be controlled by varying the solvent ratio (fig. S4), allowing compatibility with diverse printing and coating techniques, including DIW, screen printing, and dip coating. Detailed fabrication steps for ink preparation are outlined in Materials and Methods. The STAR ink formed through this process also exhibits good wettability (Fig. 2A and fig. S5) and room temperature processability (fig. S6), leading to reliable patterning, as shown in Fig. 2B (bottom). On the other hand, bare gallium often encounters unwanted merging and

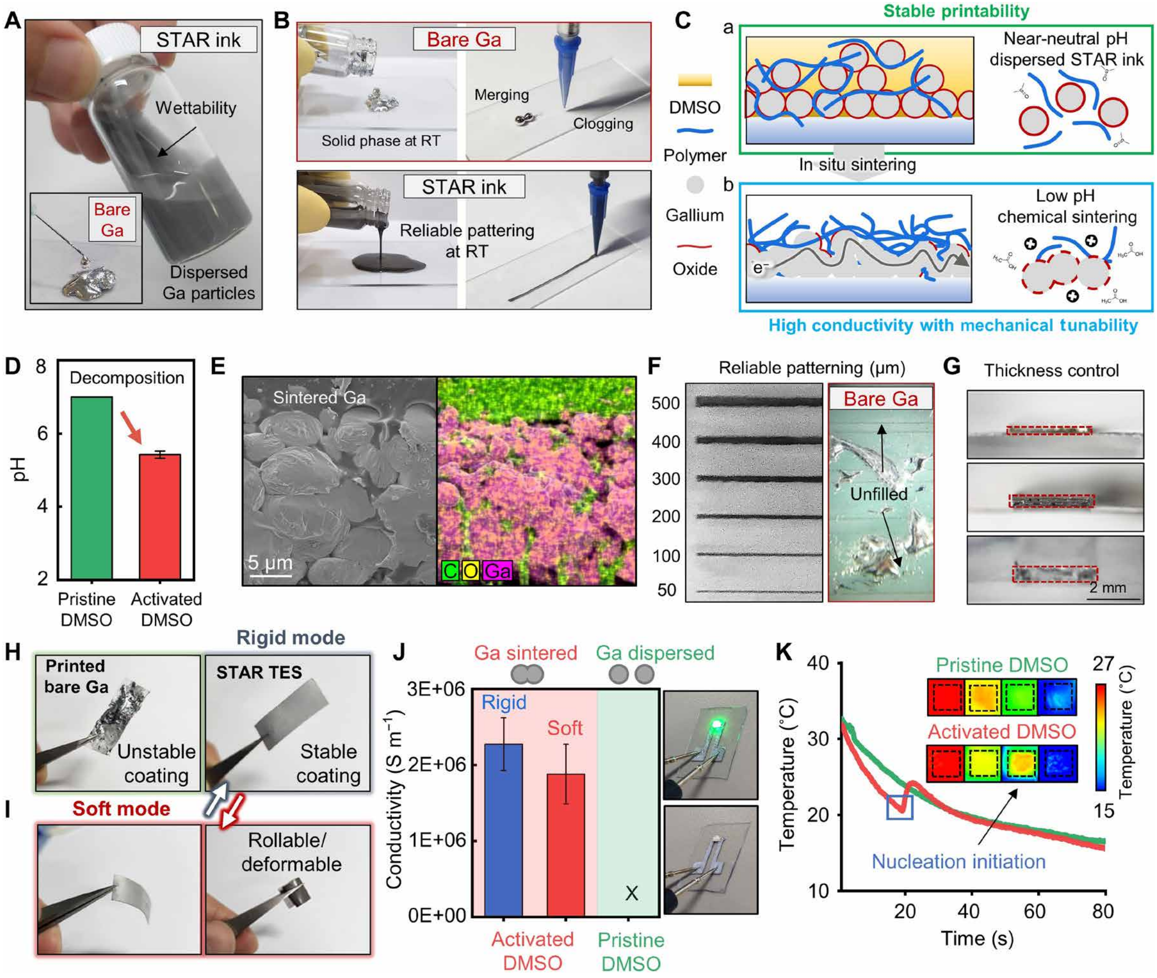

Fig. 2. Materials and characteristics of STAR ink. (**A**) Photograph of STAR ink addressing the fluidic instability inherent in bare gallium (Ga), such as its high surface tension and propensity for unwanted phase transitions during the TES fabrication process. (**B**) Photographs comparing the solution process of bare gallium and STAR ink. STAR ink shows reliable solution processing, thanks to its tunable viscosity and excellent wettability, overcoming the merging and clogging issues often encountered with bare gallium. RT, room temperature. (**C**) Schematic illustration of the sintering process of STAR ink with activated DMSO. The acidic activated DMSO reduces the oxide on dispersed gallium microparticles and induces their sintering. (**D**) pH values of pristine and activated DMSO, measured at 26.5°C. (**E**) Cross-sectional scanning electron microscopy image of STAR ink sintered with activated DMSO. (**F**) Optical images showing high-resolution patternability of STAR ink in comparison to bare gallium in screen printing. (**G**) Cross-sectional optical micrographs of STAR TES with different thicknesses. (**H**) Photographs of printed bare gallium and STAR TES in its rigid mode, demonstrating that while bare gallium tends to merge and form voids, the STAR TES maintains a stable, uniform coating without gallium agglomeration. (**I**) Photographs of STAR ink in its soft mode. (**J**) Conductivity of STAR TES fabricated with activated DMSO and pristine DMSO (left). The initial conductivity of STAR TES with activated DMSO enables its use as an interconnect to light up a light-emitting diode (LED) (top right), while STAR TES with pristine DMSO remains nonconductive after printing (bottom right). The acidic decomposed DMSO plays a crucial role in sintering gallium microparticles and establishing electrical connectivity. (**K**) Plot illustrating the liquid-to-solid phase transition of STAR TES with activated DMSO (red line) and pristine DMSO (green line). The interconnected gallium microparticles with activated DMSO promote nucleation embryos, accelerating the phase transition, unlike dispersed particles with pristine DMSO.

clogging issues in DIW due to its high surface tension and phase-change behavior (Fig. 2B, top).

To achieve electrical conductivity and stiffness tunability, the gallium particles dispersed in STAR ink [Fig. 2C (a)] must interconnect within the surrounding HPU template. In this work, we achieved this interconnection by activating DMSO to an acidic pH (5.5) through its decomposition, which facilitates the in situ sintering of STAR ink [Fig. 2C (b)]. During the tip sonication, DMSO gradually initiates decomposition, as the temperature approaches its boiling point (189°C), producing acidic compounds such as formic acid, acetic acid, methanesulfonic acid, and sulfuric acid (fig. S7) (*56*), thereby transforming DMSO into an acidic solvent (Fig. 2D and figs. S8 and S9). After printing the circuit with fabricated ink, curing at 70°C accelerates the sintering process. During solvent evaporation, the acidic environment removes gallium oxide at particle interfaces, inducing the sintering of gallium particles (Fig. 2E and fig. S10). As the DMSO fully evaporates during the curing process, STAR ink results in the formation of a STAR TES film with the desired electrical conductivity and stiffness tunability. Notably, the timing of this chemical activation is critical—it must occur during ink formation (i.e., during ultrasonic-induced dispersion). Adding an acidic solvent initially into the ink prevents the formation of gallium particles and hinders the formation of the composite ink and film (fig. S11). To elucidate the mechanism behind this process and confirm that the sintering is driven by chemical reactions rather than high temperatures alone, we conducted comparative experiments using different solvents. In addition to DMSO, we used *N*,*N*′-dimethylformamide (DMF) and *N*-methyl-2-pyrrolidone (NMP) as alternative solvents. Crucially, inks prepared with DMF and NMP, which do not provide acid at high temperature, showed no conductivity. These findings support our hypothesis that the acid generated from solvent decomposition, rather than high temperature alone, is responsible for the sintering process and subsequent conductivity (fig. S12).

Compared to conventional sintering methods, our pH-controlled chemical sintering approach is particularly advantageous for our fabrication process because it does not require additional sintering processing steps after TES fabrication. Other sintering methods are also incompatible with our system (*57*). For example, our polymer binder undergoes thermal degradation at approximately 250°C, which is lower than the typical temperatures (>300°C) required for thermal sintering (*58*). In addition, widely used mechanical sintering could lead to unwanted leakage of gallium, making it unsuitable for multilayer integration and direct integration with electronic chips (*59*, *60*).

Because of the excellent wettability and low surface tension of our STAR ink, reliable and high-resolution patterning (minimum width: 50 μm) can be realized, as shown in Fig. 2F, which facilitates the fabrication of electronic circuits in diverse dimensions (fig. S13). Furthermore, its tunable viscosity enables the fabrication of STAR ink interconnects of various thicknesses (Fig. 2G), crucial for optimized circuit designs (e.g., antenna design considering the skin effect, resistance control, etc.) and stiffness tuning in TES. STAR TES exhibits substantially better mechanical stability compared to the fluidity-induced instability of bare gallium (Fig. 2H). This stability facilitates chip integration and multilayer integration of STAR ink–based interconnects, which is impractical with bare gallium. In addition, STAR TES easily transitions to a soft mode when heated, showcasing its rollable, deformable, and stretchable characteristics (Fig. 2I).

STAR TES fabricated using activated DMSO exhibits high electrical conductivity without the need for additional postprocessing (e.g., mechanical sintering), making it a reliable material for interconnects and electrodes in various electronic systems. Postprocessing complicates the circuit fabrication process and can introduce unwanted defects, thus lowering the overall yield and manufacturability. To observe the effect of DMSO decomposition on the electrical properties of the fabricated device, a comparative study was conducted using pristine, inactivated DMSO, generated by keeping the solution cool in an ice bath during sonication. As shown in Fig. 2J, the activated DMSO-based STAR TES exhibits conductivity in both rigid and soft states, with a higher conductivity in the rigid state (rigid: 2.27×10^6 S m^{-1} and soft: 1.78×10^6 S m^{-1}), similar to the behavior observed in bare gallium (*61*). A higher conductivity in the rigid state can be attributed to the volumetric expansion of gallium during its transition from liquid to solid state, which establishes a more robust conductive pathway within the gallium interconnects. In contrast, the STAR TES fabricated using inactivated DMSO fails to sinter gallium particles (figs. S14 and S15), resulting in no electrical conductivity. This fabrication method can be broadly applied to other liquid metals such as EGaIn (fig. S16).

Besides electrical activation, sintering is also crucial for phase transition–based stiffness tuning, as depicted in Fig. 2K. The liquid-to-solid phase transition temperature of the STAR TES is influenced by the size of the constituent gallium particles; interconnected particles promote nucleation at higher temperature compared to dispersed particles. As gallium disperses into smaller particles, their reduced size exacerbates the supercooling effect, preventing its phase transition from liquid to solid state. Thus, nucleation and subsequent phase transition only occur in the device with activated DMSO as seen in movie S1. Conversely, dispersed particles in STAR ink with inactivated DMSO fail to trigger nucleation, even at 10°C (Fig. 2K). These observations underscore the importance of activated DMSO in the solution processing of STAR ink, enabling both electrical conductivity and stiffness tuning.

Systematic study on thermal, mechanical, and electrical properties of STAR TES

To evaluate the performance of STAR TES, a comprehensive study of its thermo-mechano-electrical characteristics was conducted, focusing on three essential requirements: (i) large modulus tuning, (ii) rapid and bidirectional mode transition, and (iii) stable and high electrical conductivity. Figure 3A illustrates the mechanical tunability of TES, using STAR ink interconnects integrated with a light-emitting diode (LED) on elastic silicone tape. At room temperature (~25°C), the TES maintained structural integrity under a 300-g load in its rigid state while achieving 216% elongation under the same load in its softened state. This characteristic is detailed in the stress-strain curve (Fig. 3B), which reveals substantial variations in Young's modulus between the rigid and soft modes. We studied dog bone–shaped TES printed on a stretchable silicone substrate (fig. S17), finding that in its softened mode, the TES demonstrated a Young's modulus similar to that of the silicone substrate alone. However, when rigidified, the TES exhibited a 193-fold increase in elastic modulus (rigid mode: 106.7 MPa versus soft mode: 552.3 kPa), underscoring its exceptional mechanical tunability.

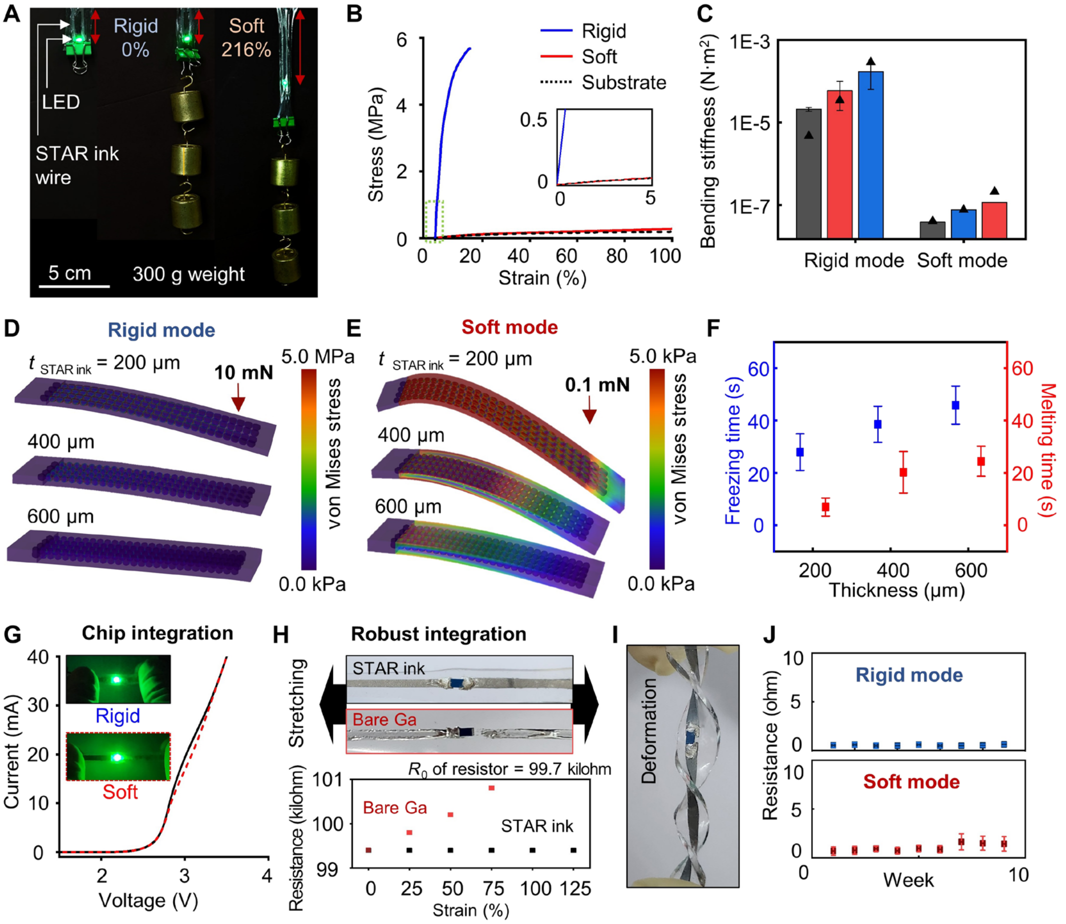

Fig. 3. Thermal, mechanical, and electrical properties of STAR ink–based TES. (**A**) Photographs of a transformative LED device in rigid and soft modes, powered by conductive STAR ink–based wires under 300-g uniaxial strain. (**B**) Stress-strain curve comparing the rigid and soft modes of a STAR ink–based TES testbed device (500-μm-thick, 2.5-mm-wide elongating part on a stretchable silicone substrate; details in fig. S11). (**C**) Bending stiffness of TES with different ink thicknesses (black: 200 μm, red: 400 μm, and blue: 600 μm) in rigid and soft modes. Bar graphs and the triangle marks indicate experimental data and simulation results, respectively. (**D** and **E**) Finite element analysis (FEA) simulation of the bending stiffness of TES [4 mm wide, 12 mm long, and encapsulated by 25-μm-thick polydimethylsiloxane (PDMS) layers on top and bottom] with various ink thicknesses (200, 400, and 600 μm) in rigid (D) and soft (E) modes, respectively. (**F**) Phase change time for liquid-to-solid (blue) and solid-to-liquid (red) transition with different thicknesses of TES ($n = 11$). (**G**) *I-V* curve of LED connected to STAR ink interconnects in the unstrained rigid mode (black line) and 100% strained soft mode (red line). (**H**) Photographs (top) and resistance values (bottom) of resistor-integrated devices fabricated using STAR ink and bare gallium under uniaxial strain. R_0, initial resistance. (**I**) Photograph of the device shown in (H), showcasing its chip integration stability in soft mode under mechanical deformation. (**J**) Resistance observation of STAR ink–based wire for 10 weeks ($n = 3$ samples).

To further characterize the mechanical tunability, we evaluated the bending stiffness of TES samples with varying thickness in rigid and soft modes through measurements (Fig. 3C) and simulations (Fig. 3, D and E). TES samples with thicknesses of 200, 400, and 600 μm, each measuring 4 mm in width and 12 mm in length, were screen printed with STAR ink and encapsulated between 25-μm-thick polydimethylsiloxane (PDMS) layers on the top and bottom. Both simulated and experimental results demonstrated a notable increase in a stiffness tuning ratio with increasing thickness. For instance, 600-μm-thick samples exhibited a stiffness tuning ratio of 1465, with substantial differences in bending stiffness between the rigid (1.69×10^{-4} N·m^2) and soft (1.55×10^{-7} N·m^2) modes. This high stiffness tuning ratio of STAR TES highlights its adaptability and suitability for applications requiring substantial changes in shape and mechanical properties.

To investigate the bidirectional mode conversion characteristic, we thoroughly explored the phase transition dynamics of STAR TES. We prepared TES samples with varying STAR ink thicknesses (200, 400, and 600 μm) via screen printing to examine the relationship between device thickness and phase transition kinetics. The samples were subjected to freezing at 0°C and thawing at 50°C. Figure 3F and fig. S18 illustrate the phase transition times and phase change curves for these samples, respectively, revealing a proportional relationship between the STAR ink thickness and phase transition duration. This relationship can be explained by heat transfer principles, specifically Fourier's law of conduction (*34*). The phase transition time ($t_{\text{transition}}$) can be expressed as $t_{\text{transition}} \propto t_{\text{encap}} \cdot t_{\text{STAR ink}} / (T_{\text{th}} - T_{\text{m}})$ where t_{encap} is the thickness of the encapsulant, $t_{\text{STAR ink}}$ is the thickness of the STAR ink layer, T_{th} is the thawing temperature, and T_{m} is the melting point of STAR TES. This equation highlights the critical role of STAR ink thickness in determining the speed of mode conversion between soft and rigid states. We observed slightly extended solidification times compared to melting times due to the supercooling phenomenon (fig. S14C) (*29*, *33*). Despite this, efficient, well-controlled bidirectional transitions were achieved across all sample thicknesses. The thinnest 200-μm sample exhibited particularly swift transitions, melting in just 7 s and freezing in 28 s. This bidirectional transition capability, coupled with substantial modulus change, underscores the potential of STAR TES for applications requiring mechanical adaptation.

Stable electrical conductivity and robust integration of STAR TES with electronic chips are crucial for practical TES implementation. The mechanical durability of STAR TES ensures reliable integration of conventional electronic components, such as an LED (Fig. 3G), functioning reliably in both rigid and soft states. Figure 3H demonstrates the STAR TES's superior performance over bare gallium in maintaining stable electrical connections under large uniaxial strain (more than 125%), with resistor-integrated devices showing consistent resistance values. This stability endures complex deformations, such as twisting, without affecting the integrated chip in the soft mode (Fig. 3I and fig. S19), highlighting STAR TES's ability to maintain its electrical function under extreme physical stresses. In contrast, the fluidity of bare gallium poses challenges for chip integration, leading to unstable electrical connections (fig. S20). STAR TES maintains stable conductance even under extreme conditions, exhibiting only a 2.14-ohm change in resistance at 1000% strain for a 600-μm sample in its soft mode (figs. S21 and S22) and enduring more than 10,000 cycles of 100% strain with minimal resistance fluctuation (fig. S23). Even after rigid STAR TES fractured under 50% strain, they reconnect upon heating and restore their conductivity (fig. S24). Furthermore, a 10-week longitudinal study confirms its sustained electrical stability (Fig. 3J), while consistent electrical and mechanical performance measurements under 100 repeated temperature cycles (fig. S25) demonstrate reliable TES circuit operation during both repeated and extended use in both rigid and soft modes. The fabricated STAR ink itself maintains stable electrical and mechanical properties for up to 3 days, allowing for consistent TES production within a time frame sufficient for practical manufacturing processes (fig. S26). For ensuring ink batch-to-batch reproducibility, 20 STAR TES from 20 different batches had their resistance (for electrical performance) and bending stiffness (for mechanical performance) evaluated in both rigid and soft modes, demonstrating excellent uniformity with minimal variation across all samples (fig. S27).

Multilayer T-PCB with design complexity of standard PCBs

The introduction of a solution-processible STAR ink offers an approach and methodology for developing T-PCB, addressing the limitations of traditional integrated and multifunctional electronics with invariant mechanical properties. T-PCBs enhance the adaptability of conventional PCBs by enabling customizable stiffness for specific functions, thereby expanding their application range. Engineered to meet key features of conventional PCBs, our T-PCBs achieve minimal line and spacing widths of 50 μm, via hole dimensions of 50 μm, and the ability to incorporate multiple layers, as detailed in Fig. 4A. This high resolution is achieved through stencil mask patterning, where the high viscosity of STAR ink prevents lateral spreading, enabling precise 50-μm linewidths. With more precise stencil mask designs, even higher-resolution patterns could be achieved with our ink. A detailed comparison of T-PCBs with commercial rigid and flexible PCBs is provided in table S2. Notably, our STAR ink–based T-PCB achieves a reduction of 34.4 and 16.7% in line/spacing thickness compared to traditional rigid and flexible PCBs, respectively.

Leveraging the distinctive mechanical properties of STAR ink, we have developed a STAR ink–based multilayer T-PCB for multifunctional personal electronics. The high electrical conductivity, microscale printability, and mechanical stability of STAR ink facilitate the development of a robust, high-resolution, and multilayered T-PCB, comparable to the complexity of standard PCBs. Configured with 30 SMDs and 12 vertical interconnect accesses with three circuit layers, as shown in Fig. 4B, the T-PCB adeptly serves dual purposes (i.e., computing and health monitoring), converting between rigid, portable and soft, wearable forms. As a single integrated system, the device can be used as a handheld or portable calculator in rigid mode or as a wearable photoplethysmography (PPG) sensor to monitor blood pulse rate in soft mode. Here, the functional mode selection between computing and health monitoring is facilitated by a simple button press, displaying either a calculator or heart rate sensing function on the organic light emitting diode (OLED) screen, and the device's stiffness tuning is achieved by body temperature. Figure 4C illustrates body-temperature softening of T-PCB, highlighting the distinct advantages of each state: (i) The rigid state offers solid interfaces that maximize convenience of use similar to traditional electronics, whereas (ii) the soft state provides surface conformability and mechanical adaptability for comfortable wear and intimate skin interfacing for high-fidelity physiological sensing. This unique transformative feature allows users to use the optimal form factor for desired applications. Details in the circuit design and software code are available in fig. S28, note S1, and Materials and Methods.

To elucidate the thermal characteristics governing T-PCB's transformation, we conducted a comprehensive analysis of its phase transitions using an infrared (IR) camera. Figure 4D depicts the T-PCB's temperature response during thawing at 50°C, where the bottommost circuit layer initiates a rigid-to-soft transition, taking 7.042 s for complete phase change, followed by the topmost layer transition, which takes slightly longer (8.001 s) due to the delayed heat transfer from the heater below. Figure 4E illustrates the freezing response at 0°C, showing a thermal behavior similar to thawing but with an additional supercooling phase before gallium initiates the nucleation process. In this process, the bottommost layer solidifies in 8.960 s, while the topmost layer takes 10.562 s. Despite supercooling, the transition from soft to rigid mode takes place rapidly due to the interconnected gallium structure, which allows nucleation embryos to remain at temperatures above the melting point (*33*). This result reveals that the influence of incorporating additional circuit layers (trace thickness: 500 μm) on phase transition time is not substantial. Nonetheless, careful thickness control would be needed to optimize T-PCB's rigidity (fig. S29) and mode conversion time, catering to meet diverse application needs.

The bidirectional conversion capability of T-PCB between rigid and soft modes broadens the utility of electronics, as showcased in Fig. 4F and movie S2. In its rigid state, T-PCB is suited to handheld or tabletop computing, akin to smartphones and tablets (fig. S30A), whereas its soft mode is ideal for wearable applications, ensuring comfortable and adaptable wear on various body parts due to its conformability (fig. S30B). In addition, its deformable nature along with STAR ink's mechanical stability enables compact storage, setting it apart from bulk gallium-based TES, which suffers from fluidic instability in soft mode (fig. S31), underscoring the high interfacial stability and robustness of STAR ink–based T-PCBs in their practical applications.

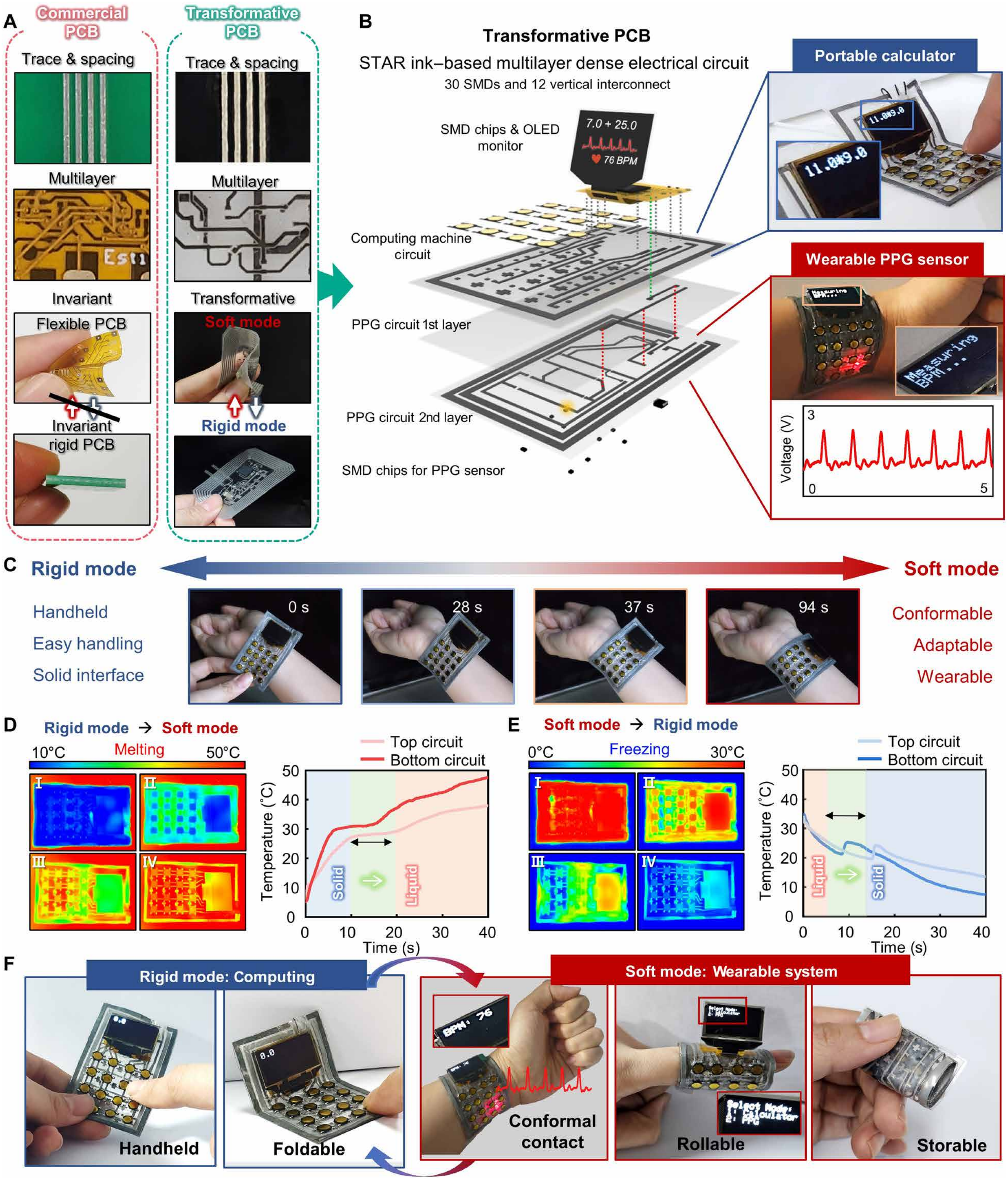

Fig. 4. Multilayer T-PCB based on STAR ink, exhibiting design complexity comparable to standard PCBs. (**A**) Photograph illustrating key feature comparisons between conventional PCB and T-PCB based on STAR ink. (**B**) Exploded view schematic diagram (left) and photographs (right) of a multilayer T-PCB, working as a portable calculator in rigid mode and a wearable photoplethysmography (PPG) sensor in soft mode. BPM, beats per minute. (**C**) Photographs showcasing the seamless mode transition of the T-PCB from the rigid handheld to the soft wearable device, triggered by body temperature. The bidirectional mode convertibility provides portability and ease of use in rigid mode while offering deformability with conformal contact in soft mode. (**D** and **E**) Infrared (IR) images (left) and the corresponding phase transition plots (right) of the multilayered T-PCB during rigid-to-soft conversion (D) and soft-to-rigid conversion (E). (**F**) Photographs demonstrating the practical utilities of the T-PCB in convertible dual modes tailored for specific uses: the rigid mode for handheld calculating and the soft mode for wearable PPG sensing.

Body-temperature softening implantable probe for multifunctional neural interfacing

While T-PCBs demonstrate potential for everyday electronics, the stiffness tunability of STAR TES extends its usage into implantable neural devices. Flexible and stretchable neural probes have garnered attention for their superior biomechanical compatibility with brain tissue (*62*–*64*). They not only reduce foreign body response by accommodating brain micromotion but also offer highly stable performance against external mechanical stresses in the long term (*65*, *66*). However, their softness, while advantageous postimplantation, poses a critical challenge: buckling during insertion, which hinders deep brain penetration. Our STAR ink–based body-temperature softening implantable probe overcomes this limitation. Through a simple STAR ink coating process, extremely soft probes transform into reliable deep brain implants by maintaining rigidity during implantation and facilitating precise targeting of deep brain regions. However, upon reaching body temperature postinsertion, the probes transition to a soft state, conforming to brain tissue and minimizing micromotion effects. Unlike previous stimuli-responsive materials used in implantable or injectable devices, which serve only as mechanical frameworks (*29*, *34*), STAR ink functions as both a stiffness-varying scaffold and a conductive electrode material, eliminating the need for separate conductive components for biosensing applications. This dual functionality not only resolves the implantability-tissue compatibility trade-off but also expands the probe's capabilities, enabling simultaneous optogenetics and neural recording, as demonstrated in Fig. 5A.

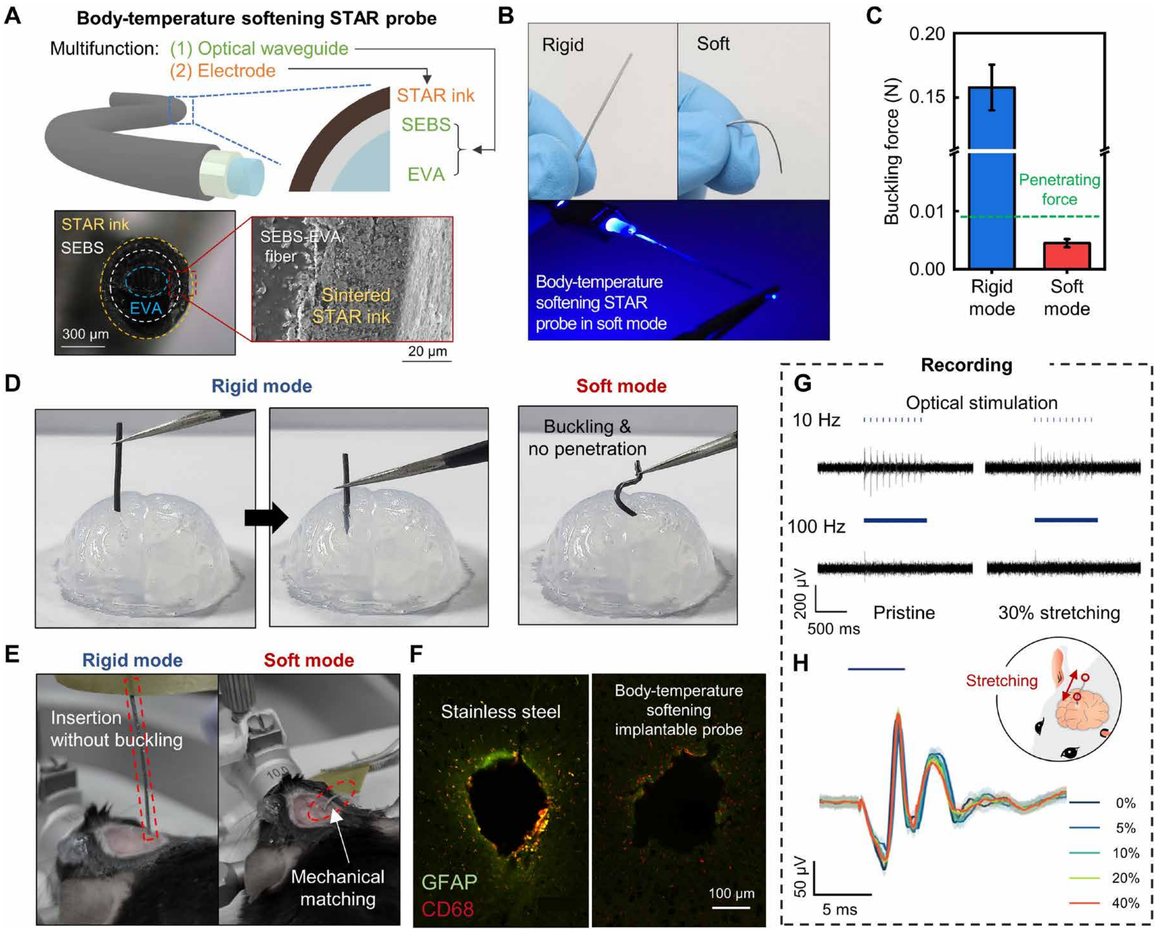

Fig. 5. Body-temperature softening implantable probe enabled by STAR ink for multifunctional neural interface. (**A**) Schematic illustration (top) and optical images (bottom) of a body-temperature softening implantable probe created through coating of STAR ink on a polymeric optical fiber. The probe features an ethylene-vinyl acetate (EVA) core and poly(ethylene-ran-butylene)-block-polystyrene (SEBS) cladding for light delivery, along with a STAR ink coating layer that adjusts stiffness and enables electrical recording, for simultaneous optogenetic stimulation and neural recording. (**B**) Photograph of the softening probe in rigid (left) and soft modes (right). Bottom image shows a stretchable neural probe in its soft mode. (**C**) Buckling force of the probe in rigid and soft modes. The probe's buckling force surpasses the force needed for brain penetration in rigid mode but is lower in soft mode, indicating that penetration is feasible only in the rigid mode. (**D**) Photograph demonstrating injection of the probe in rigid and soft modes. Only the rigid mode device can penetrate the phantom brain tissue (0.6 wt % agarose gel). (**E**) Photographs during insertion in rigid mode (left) and after insertion, converted to the soft mode by body temperature (right). (**F**) Representative confocal images of brain tissue slices, highlighting substantially less foreign body responses of the STAR ink probe (right) compared to the stainless steel probe (left) in the implanted brain region. Immunohistochemistry staining shows 4′,6-diamidino-2-phenylindole (blue) and expression of GFAP (glial fibrillary acidic protein; green) and CD68 (cluster of differentiation 68 protein; red). (**G**) In vivo recording with STAR-based probe. Evoked potentials in response to 10-Hz (top) and 100-Hz (bottom) optical stimulation (10 pulses) without (left) and with 30% strain of the probe (right). (**H**) The averaged evoked potentials measured across different probe strain levels, with each color representing a distinct level of strain ($n = 100$).

For the fabrication of the probe, initially, a soft waveguide fiber was created using poly(ethylene-ran-butylene)-block-polystyrene (SEBS) and ethylene-vinyl acetate (EVA) through thermal drawing (fig. S32). The fiber was then dipcoated with the STAR ink with optimized viscosity (fig. S33) to introduce both stiffness tunability and electrical conductance. Subsequently, a thin layer of poly(3,4-ethylenedioxythiophene) polystyrene sulfonate (PEDOT:PSS) was applied on top to ensure the biocompatibility of the electrode. The resulting STAR ink–coated neural probe (STAR probe) exhibits excellent mechanical tunability, reliable light delivery (Fig. 5, B and C), and low electrical resistance (~0.7 ohm/cm).

The STAR probe demonstrates a marked tuning in buckling force between its rigid and soft modes (0.158 N in rigid mode versus 0.0045 N in soft mode; Fig. 5C). Specifically, the strong bending force of the probe in the rigid mode allows facile injection into brain tissue phantom (0.6 wt % agarose gel), while the softened probe cannot penetrate it (Fig. 5D and fig. S34). The versatility of the STAR probe for neural interfacing is further confirmed through animal experiments with mice. The STAR probe, upon reliable implantation into brain tissue in rigid mode, softened by body temperature, offering excellent tissue adaptability (Fig. 5E). The biomechanical compatibility of the softened probe resulted in a substantially lower immune response, compared to the rigid stainless steel probes, ensuring biocompatible, chronic neural interfacing (Fig. 5F and fig. S35).

The multifunctional capability of the STAR probe was verified through simultaneous optogenetics and neural recording (*67*). Using the probe, we successfully recorded optically evoked potentials from the hippocampus CA1 regions of Thy1:channelrhodopsin 2 (ChR2)–yellow fluorescent protein mice (Fig. 5G). The frequency-dependent responses at 10 and 100 Hz further confirmed the neuronal firings in response to optical stimulation, considering ChR2 kinetics (*68*). Furthermore, the STAR probe exhibited performance under mechanical stress, maintaining stable neural signal recording even when subjected to stretching (Fig. 5H). Because of the reliability of the STAR probe, it maintained the peak amplitude of evoked potential up to 40% stretching. This deformability is crucial for the stable performance of the neural probe in the long term, in the presence of external force or displacement. Together, these findings highlight the versatile processability (e.g., coating and printing) and multifaceted functional attributes of STAR ink, enabling it to serve as both a mechanical scaffold and an electrical device. Consequently, the unique combination of properties positions STAR ink as a promising material for a broad spectrum of advanced bioelectronic applications.

DISCUSSION

This study presents an innovative solution to the challenges faced in transformative electronics constructed using bulk liquid metal. Low–melting-point metals, such as gallium, have been considered effective for TES and shape-morphing electronics. However, their inherent challenges, such as fluidic instability, high surface tension, and unwanted phase transitions, have limited their use in TES. Our STAR ink addresses these limitations, harnessing the full potential of gallium for TES applications. This solution-state ink, composed of micro-sized gallium particles dispersed in an HPU template, exhibits optimal rheological properties that enable high-resolution patterning (down to 50 μm) and multilayer printing. Its room temperature processing capability ensures unmatched compatibility with a variety of fabrication methods, including screen printing and dip coating, facilitating large-scale batch production and precise coating of complex 3D structures.

TES, fabricated with STAR ink, combines high electrical conductivity with mechanical tunability, integrating electrical and mechanical functionalities into a single, cohesive unit, thus eliminating the need for separate stiffness-tunable frameworks. We demonstrated the versatility of STAR ink through two applications: a multilayered high-density T-PCB and a body-temperature softening implantable probe for multifunctional neural interfacing. The T-PCB, featuring ~50-μm linewidth, seamlessly transitions between rigid portable electronics and flexible wearable health care devices, while the neural probe offers both easy surgical handling and postimplantation tissue adaptability. By bridging the gap between soft and rigid electronics, our ink opens pioneering avenues for reconfigurable electronic systems that can dynamically respond to diverse functional requirements. We believe that this breakthrough has the potential to revolutionize wearable and implantable technologies, paving the way for an advanced generation of multifunctional, shape-adaptable electronic devices across various fields, including consumer electronics, biomedical applications, and robotics.

MATERIALS AND METHODS

Materials

Unless otherwise stated, all chemicals used in this work were used without further purification. Gallium was purchased from Indium Corporation, and hydrophilic polymer (HPU, HydroThane AL 93A) was obtained from ULTRUS. DMSO (D5879) was purchased from Sigma-Aldrich.

Fabrication of STAR ink

A solution of HPU was prepared by dissolving 7 g of HPU in 45 ml of DMSO at 70°C with a stirring bar for 8 hours. Subsequently, 1.2 ml of liquid gallium was added to 9 ml of the prepared HPU solution. The mixture was then tip sonicated (13-mm extender; VC-505, Sonics & Materials) at 40% amplitude for 5 min to ensure homogeneous dispersion of gallium within the solution.

Various printing and processing methods for STAR ink based on solution process

Using solution-processible STAR ink, several printing techniques can be used, including screen printing, standing film printing, and dip coating.

Screen printing

A mask was created using thermal release tape (T&A Co.), which was patterned with an ultraviolet (UV) laser cutter (MD-U 3-axis UV Laser Marker, Keyence). The minimum linewidth of the stencil mask using a UV laser cutter was 50 μm. This mask was applied to an elastic silicone tape substrate, followed by the screen printing of STAR ink using a rubber blade. The screen-printed sample was then cured on a hot plate at 70°C for 5 min. After curing, the thermal release tape lost its adhesiveness and was easily peeled off. The substrate was further cured at 70°C to evaporate the DMSO solvent for 10 hours, finalizing the TES formation.

Standing film printing and laser patterning

STAR ink was poured onto a PDMS-coated wafer and cured at 70°C for 10 hours. Following DMSO evaporation, the STAR TES was patterned using a UV laser cutter (MD-U 3-axis UV Laser Marker, Keyence) according to a computer-aided design (CAD) (.dwg file).

Dip coating

A desired structure was immersed in STAR ink and then cured in an oven at 70°C for 10 hours. This dipping and curing cycle were repeated to achieve a thicker coating, enhancing the structural integrity of the TES.

Electrical and electromechanical characterization

The resistance of STAR TES was determined using a four-point probe (2420 SourceMeter, Keithley). The conductivity, which is the reciprocal of resistivity, was calculated using the formula: $\rho = R \times w \times t/l$, where ρ represents the resistivity, R is resistance, w is the sample's width, t is its thickness, and l is its length. The dimensions of the sample were thickness = 0.003 cm, width = 0.2 cm, and length = 0.1 cm. The four-point probe measurement was conducted with a 10-mA current range and a 2.1-V voltage limit. For measuring resistance in relation to stretchability and during cycle tests, a dog bone–shaped TES with a thickness of 200 μm on an elastic silicone tape substrate was used. The resistance changes in response to strain were monitored in real time using an inductance (L), capacitance (C), and resistance (R) (LCR) meter (4284A, HP) coupled with a force gauge (Mark-10, Series-5). In addition, the long-term stability and robust integration tests were evaluated using the LCR meter to directly measure resistance. The samples were subjected to freezing at 0°C for the rigid mode test and thawing at 50°C for the soft mode test.

Bending stiffness measurement

Bending stiffness of STAR TES was obtained through deflection measurements under an applied force. STAR TES (dimensions: 0.4 cm width and 1.2 cm length; thicknesses: 200, 400, and 600 μm) was fabricated via screen printing of STAR ink, encapsulated between 25-μm-thick PDMS layers on the top and bottom. In the experimental setup, one end of the TES was fixed, while the other end was subjected to external force using a force gauge (Mark-10, Series-5). The bending stiffness ($E{\cdot}I$, where E is Young's modulus and I is area moment of inertia) was calculated using the beam deflection equation $E{\cdot}I = FL^3/3\Delta z$, where F is the applied force, L is the sample length, and Δz is the measured deflection. The samples were subjected to freezing at 0°C for the rigid mode test and thawing at 50°C for the soft mode test.

Mechanical modeling and finite element analysis

Bending stiffness of STAR TES was simulated using finite element analysis (FEA) software (COMSOL Multiphysics, COMSOL Inc.). 3D models were constructed to replicate the experimental TES structure, comprising interconnected gallium particles in a polyurethane matrix (dimensions: 0.4 cm width and 1.2 cm length; thicknesses: 200, 400, and 600 μm), with 25-μm-thick PDMS encapsulation layers on both surfaces. Simulations were conducted by applying downward pressures of 10 and 0.1 mN for rigid and soft modes, respectively. Deflection data from these simulations were used to calculate bending stiffness using the same equation as in the experimental analysis.

Phase transition observation of STAR TES

To observe the phase transitions of the STAR ink–based TES, an IR camera (A655sc, FLIR) was used, with data analyzed using the FLIR software program. For the melting process, the sample was initially maintained at room temperature (25°C) and then heated on a hot plate up to 50°C. Conversely, for the freezing process, the sample was cooled using a cool plate down to 0°C (CP-200TT, TE Technology).

Dual-mode circuit design and signal processing for PPG sensing and calculation in a T-PCB

The circuit architecture of the T-PCB, as shown in fig. S18, included dual functions: an electronic calculator and a PPG sensor. It incorporated a 0.96-inch (24.38-mm) OLED display (zjy026, ICBANQ) to visualize both numerical calculations and heart rate data derived from PPG signals. The calculator functionality was managed through a 4-by-4 push-button switch array, comprising 10 numeric (0 to 9) and 6 functional buttons (+, −, ×, %, =, and mode selection), connected to eight inputs on an Atmega328P-AU microcontroller (Mouser). The PPG sensor measured blood volume changes via red light (632 nm) emitted from an LED (755-CSL1901VW1, Kingbright), regulated by a 100-ohm resistor (ERA-2ARB101X) and detected by a photodiode (630 nm; ALS-PT19-315C/L177/TR8, Everlight). The photodiode's output current was transformed into voltage by a 10-kilohm resistor (RC1005F103CS, Samsung Electro-Mechanics). The signal-to-noise ratio was enhanced by a capacitor network acting as a low-pass filter with a 20-Hz cutoff to attenuate high-frequency noise. The ac PPG signals were then amplified 1700 times using an inverting amplifier setup that included a 2.7-kilohm resistor (ERJ-2GEJ272X, Panasonic), a 4.8-megohm resistor (RMCF0402FT4M75, Stackpole Electronics), and an operational amplifier (TSV6192IST, STMicroelectronics). In addition, the dc offset was stabilized at half the supply voltage using two 100-kilohm resistors (ERA-2AED104X, Panasonic). The T-PCB module processed raw signals directly through the microcontroller to calculate heart rate. The setup ensured that output from both the calculator and the PPG sensor was concurrently displayed on the OLED screen, facilitating immediate feedback. The detailed Arduino code is available in note S1.

Fabrication of STAR probe

The fabrication process started with the preparation of a macroscopic "preform" with the desired structure of the microscopic fiber. This preform consisted of EVA as the core, surrounded by SEBS as the cladding. The preform was then heated and drawn at temperatures ranging from 150° to 170°C using a furnace and capstan within our tower system, a method known as the thermal drawing process (TDP). Through TDP, we successfully manufactured a soft waveguiding fiber with a cross section of 300 μm. This fiber was subsequently dipcoated with high-viscosity STAR ink to form an electrode. The fabrication was completed by annealing the coated fiber at 80°C in a vacuum oven for 10 hours.

In vivo experiment

All application procedures involving the mouse model were conducted with approval from the Institutional Animal Care and Use Committee (IACUC) of Korea Advanced Institute of Science and Technology (KAIST). The experiments used the Thy1 promoter–ChR2 transgenic mouse line (Thy1::ChR2 mice). The STAR probe was implanted using a stereotaxic frame (Digital Stereotaxic Instrument 68025, RWD Life Science Corp., Shenzhen, China). Extracellular electrophysiological recordings were conducted at a filtering frequency ranging from 300 Hz to 5000 Hz and a sampling rate of 24,414 Hz.

Experiments on human subjects

All experiments on human skin were performed under approval from the Institutional Review Board at KAIST (protocol number: KH2018-35) and received informed consent from the volunteer individuals.

Experiments on animal subjects

All experimental procedures involving the mouse model were approved by the IACUC at KAIST (KA2023-036).

Statistical and data analysis

The data presented in Figs. 2 (D and J), 3 (C, F, and J), and 5C represent means with SDs, with sample sizes of $n = 5$, 4, 5, 5, 3, and 6, respectively. Figure S25 reports data as means ± standard deviation (SD) for $n = 4$ animals per implant. All data were analyzed with Origin (OriginPro).

Supplementary Materials

The PDF file includes:

Tables S1 and S2
Note S1
Figs. S1 to S35
Legends for movies S1 and S2

Other Supplementary Material for this manuscript includes the following:

Movies S1 and S2

REFERENCES AND NOTES

1. P.-C. Shen, C. Su, Y. Lin, A.-S. Chou, C.-C. Cheng, J.-H. Park, M.-H. Chiu, A.-Y. Lu, H.-L. Tang, M. M. Tavakoli, G. Pitner, X. Ji, Z. Cai, N. Mao, J. Wang, V. Tung, J. Li, J. Bokor, A. Zettl, C.-I. Wu, T. Palacios, L.-J. Li, J. Kong, Ultralow contact resistance between semimetal and monolayer semiconductors. *Nature* **593**, 211–217 (2021).
2. W. Jin, C.-Y. Yang, R. Pau, Q. Wang, E. K. Tekelenburg, H.-Y. Wu, Z. Wu, S. Y. Jeong, F. Pitzalis, T. Liu, Q. He, Q. Li, J.-D. Huang, R. Kroon, M. Heeney, H. Y. Woo, A. Mura, A. Motta, A. Facchetti, M. Fahlman, M. A. Loi, S. Fabiano, Photocatalytic doping of organic semiconductors. *Nature* **630**, 96–101 (2024).
3. X. Duan, C. Niu, V. Sahi, J. Chen, J. W. Parce, S. Empedocles, J. L. Goldman, High-performance thin-film transistors using semiconductor nanowires and nanoribbons. *Nature* **425**, 274–278 (2003).
4. T. Okamoto, S. Kumagai, E. Fukuzaki, H. Ishii, G. Watanabe, N. Niitsu, T. Annaka, M. Yamagishi, Y. Tani, H. Sugiura, T. Watanabe, S. Watanabe, J. Takeya, Robust, high-performance n-type organic semiconductors. *Sci. Adv.* **6**, eaaz0632 (2020).
5. S. Chae, W. J. Choi, L. J. Nebel, C. H. Cho, Q. A. Besford, A. Knapp, P. Makushko, Y. Zabila, O. Pylypovskyi, M. W. Jeong, S. Avdoshenko, O. Sander, D. Makarov, Y. J. Chung, A. Fery, J. Y. Oh, T. I. Lee, Kinetically controlled metal-elastomer nanophases for environmentally resilient stretchable electronics. *Nat. Commun.* **15**, 3071 (2024).
6. P. Xu, S. Wang, A. Lin, H.-K. Min, Z. Zhou, W. Dou, Y. Sun, X. Huang, H. Tran, X. Liu, Conductive and elastic bottlebrush elastomers for ultrasoft electronics. *Nat. Commun.* **14**, 623 (2023).
7. D.-H. Kim, N. Lu, R. Ma, Y.-S. Kim, R.-H. Kim, S. Wang, J. Wu, S. M. Won, H. Tao, A. Islam, K. J. Yu, T. Kim, R. Chowdhury, M. Ying, L. Xu, M. Li, H.-J. Chung, H. Keum, M. McCormick, P. Liu, Y.-W. Zhang, F. G. Omenetto, Y. Huang, T. Coleman, J. A. Rogers, Epidermal electronics. *Science* **333**, 838–843 (2011).
8. D. Zhong, C. Wu, Y. Jiang, Y. Yuan, M. Kim, Y. Nishio, C.-C. Shih, W. Wang, J.-C. Lai, X. Ji, T. Z. Gao, Y.-X. Wang, C. Xu, Y. Zheng, Z. Yu, H. Gong, N. Matsuhisa, C. Zhao, Y. Lei, D. Liu, S. Zhang, Y. Ochiai, S. Liu, S. Wei, J. B.-H. Tok, Z. Bao, High-speed and large-scale intrinsically stretchable integrated circuits. *Nature* **627**, 313–320 (2024).
9. M. Kaltenbrunner, T. Sekitani, J. Reeder, T. Yokota, K. Kuribara, T. Tokuhara, M. Drack, R. Schwödiauer, I. Graz, S. Bauer-Gogonea, S. Bauer, T. Someya, An ultra-lightweight design for imperceptible plastic electronics. *Nature* **499**, 458–463 (2013).
10. J.-W. Jeong, J. G. McCall, G. Shin, Y. Zhang, R. Al-Hasani, M. Kim, S. Li, J. Y. Sim, K.-I. Jang, Y. Shi, D. Y. Hong, Y. Liu, G. P. Schmitz, L. Xia, Z. He, P. Gamble, W. Z. Ray, Y. Huang, M. R. Bruchas, J. A. Rogers, Wireless optofluidic systems for programmable in vivo pharmacology and optogenetics. *Cell* **162**, 662–674 (2015).
11. W. Lee, H. Kim, I. Kang, H. Park, J. Jung, H. Lee, H. Park, J. S. Park, J. M. Yuk, S. Ryu, J.-W. Jeong, J. Kang, Universal assembly of liquid metal particles in polymers enables elastic printed circuit board. *Science* **378**, 637–641 (2022).
12. G.-H. Lee, D. H. Lee, W. Jeon, J. Yoon, K. Ahn, K. S. Nam, M. Kim, J. K. Kim, Y. H. Koo, J. Joo, W. Jung, J. Lee, J. Nam, S. Park, J.-W. Jeong, S. Park, Conductance stable and mechanically durable bi-layer EGaIn composite-coated stretchable fiber for 1D bioelectronics. *Nat. Commun.* **14**, 4173 (2023).
13. J. Lv, G. Thangavel, Y. Xin, D. Gao, W. C. Poh, S. Chen, P. S. Lee, Printed sustainable elastomeric conductor for soft electronics. *Nat. Commun.* **14**, 7132 (2023).
14. H. C. Ates, P. Q. Nguyen, L. Gonzalez-Macia, E. Morales-Narváez, F. Güder, J. J. Collins, C. Dincer, End-to-end design of wearable sensors. *Nat. Rev. Mater.* **7**, 887–907 (2022).
15. S. M. A. Iqbal, I. Mahgoub, E. Du, M. A. Leavitt, W. Asghar, Advances in healthcare wearable devices. *npj Flex. Electron.* **5**, 9 (2021).
16. C. Bao, Z. Yuan, W. Niu, J. Yang, Z. Wang, T. Yu, J. Wang, F. Gao, A multifunctional display based on photo-responsive perovskite light-emitting diodes. *Nat. Electron.* **7**, 375–382 (2024).
17. M. Dai, Z. Song, C.-H. Lin, Y. Dong, T. Wu, J. Chu, Multi-functional multi-gate one-transistor process-in-memory electronics with foundry processing and footprint reduction. *Commun. Mater.* **3**, 41 (2022).
18. A. Sahasrabudhe, L. E. Rupprecht, S. Orguc, T. Khudiyev, T. Tanaka, J. Sands, W. Zhu, A. Tabet, M. Manthey, H. Allen, G. Loke, M.-J. Antonini, D. Rosenfeld, J. Park, I. C. Garwood, W. Yan, F. Niroui, Y. Fink, A. Chandrakasan, D. V. Bohórquez, P. Anikeeva, Multifunctional microelectronic fibers enable wireless modulation of gut and brain neural circuits. *Nat. Biotechnol.* **42**, 892–904 (2024).
19. M. Cai, Z. Jiao, S. Nie, C. Wang, J. Zou, J. Song, A multifunctional electronic skin based on patterned metal films for tactile sensing with a broad linear response range. *Sci. Adv.* **7**, eabl8313 (2021).
20. L. Luan, X. Wei, Z. Zhao, J. J. Siegel, O. Potnis, C. A. Tuppen, S. Lin, S. Kazmi, R. A. Fowler, S. Holloway, A. K. Dunn, R. A. Chitwood, C. Xie, Ultraflexible nanoelectronic probes form reliable, glial scar–free neural integration. *Sci. Adv.* **3**, e1601966 (2017).
21. L. Tian, B. Zimmerman, A. Akhtar, K. J. Yu, M. Moore, J. Wu, R. J. Larsen, J. W. Lee, J. Li, Y. Liu, B. Metzger, S. Qu, X. Guo, K. E. Mathewson, J. A. Fan, J. Cornman, M. Fatina, Z. Xie, Y. Ma, J. Zhang, Y. Zhang, F. Dolcos, M. Fabiani, G. Gratton, T. Bretl, L. J. Hargrove, P. V. Braun, Y. Huang, J. A. Rogers, Large-area MRI-compatible epidermal electronic interfaces for prosthetic control and cognitive monitoring. *Nat. Biomed. Eng.* **3**, 194–205 (2019).
22. J.-W. Jeong, W.-H. Yeo, A. Akhtar, J. J. S. Norton, Y.-J. Kwack, S. Li, S.-Y. Jung, Y. Su, W. Lee, J. Xia, H. Cheng, Y. Huang, W.-S. Choi, T. Bretl, J. A. Rogers, Materials and optimized designs for human-machine interfaces via epidermal electronics. *Adv. Mater.* **25**, 6839–6846 (2013).
23. D. Wang, H. Hu, S. Li, H. Tian, W. Fan, X. Li, X. Chen, A. C. Taylor, J. Shao, Sensing-triggered stiffness-tunable smart adhesives. *Sci. Adv.* **9**, eadf4051 (2023).
24. Y. Wang, L. Li, D. Hofmann, J. E. Andrade, C. Daraio, Structured fabrics with tunable mechanical properties. *Nature* **596**, 238–243 (2021).
25. S. Oh, S. Lee, S. W. Kim, C. Y. Kim, E. Y. Jeong, J. Lee, D. A. Kwon, J.-W. Jeong, Softening implantable bioelectronics: Material designs, applications, and future directions. *Biosens. Bioelectron.* **258**, 116328 (2024).
26. G. Yun, T. Cole, Y. Zhang, J. Zheng, S. Sun, Y. Ou-yang, J. Shu, H. Lu, Q. Zhang, Y. Wang, D. Pham, T. Hasan, W. Li, S. Zhang, S.-Y. Tang, Electro-mechano responsive elastomers with self-tunable conductivity and stiffness. *Sci. Adv.* **9**, eadf1141 (2023).
27. S.-H. Byun, J. Y. Sim, K.-C. Agno, J.-W. Jeong, Materials and manufacturing strategies for mechanically transformative electronics. *Mater. Today Adv.* **7**, 100089 (2020).
28. D. A. Kwon, S. Lee, C. Y. Kim, I. Kang, S. Park, J.-W. Jeong, Body-temperature softening electronic ink for additive manufacturing of transformative bioelectronics via direct writing. *Sci. Adv.* **10**, eadn1186 (2024).
29. K.-C. Agno, K. Yang, S.-H. Byun, S. Oh, S. Lee, H. Kim, K. Kim, S. Cho, W.-I. Jeong, J.-W. Jeong, A temperature-responsive intravenous needle that irreversibly softens on insertion. *Nat. Biomed. Eng.* **8**, 963–976 (2024).
30. S. Oh, S. Lee, S.-H. Byun, S. Lee, C. Y. Kim, J. Yea, S. Chung, S. Li, K.-I. Jang, J. Kang, J.-W. Jeong, 3D shape-morphing display enabled by electrothermally responsive, stiffness-tunable liquid metal platform with stretchable electroluminescent device. *Adv. Funct. Mater.* **33**, 2214766 (2023).
31. S. Lee, S.-H. Byun, C. Y. Kim, S. Cho, S. Park, J. Y. Sim, J.-W. Jeong, Beyond human touch perception: An adaptive robotic skin based on gallium microgranules for pressure sensory augmentation. *Adv. Mater.* **34**, 2204805 (2022).
32. S.-H. Byun, J. H. Yun, S.-Y. Heo, C. Shi, G. J. Lee, K.-C. Agno, K.-I. Jang, J. Xiao, Y. M. Song, J.-W. Jeong, Self-cooling gallium-based transformative electronics with a radiative cooler for reliable stiffness tuning in outdoor use. *Adv. Sci.* **9**, 2202549 (2022).
33. S.-H. Byun, C. S. Kim, K.-C. Agno, S. Lee, Z. Li, B. J. Cho, J.-W. Jeong, Design strategy for transformative electronic system toward rapid, bidirectional stiffness tuning using graphene and flexible thermoelectric device interfaces. *Adv. Mater.* **33**, e2007239 (2021).
34. S.-H. Byun, J. Y. Sim, Z. Zhou, J. Lee, R. Qazi, M. C. Walicki, K. E. Parker, M. P. Haney, S. H. Choi, A. Shon, G. B. Gereau, J. Bilbily, S. Li, Y. Liu, W.-H. Yeo, J. G. McCall, J. Xiao, J.-W. Jeong, Mechanically transformative electronics, sensors, and implantable devices. *Sci. Adv.* **5**, eaay0418 (2019).
35. H. M. El-Husseiny, E. A. Mady, L. Hamabe, A. Abugomaa, K. Shimada, T. Yoshida, T. Tanaka, A. Yokoi, M. Elbadawy, R. Tanaka, Smart/stimuli-responsive hydrogels: Cutting-edge platforms for tissue engineering and other biomedical applications. *Mater. Today Bio.* **13**, 100186 (2022).
36. Z. Li, Y. Zhou, T. Li, J. Zhang, H. Tian, Stimuli-responsive hydrogels: Fabrication and biomedical applications. *VIEW* **3**, 20200112 (2022).

37. S. Park, H. Yuk, R. Zhao, Y. S. Yim, E. W. Woldeghebriel, J. Kang, A. Canales, Y. Fink, G. B. Choi, X. Zhao, P. Anikeeva, Adaptive and multifunctional hydrogel hybrid probes for long-term sensing and modulation of neural activity. *Nat. Commun.* **12**, 3435 (2021).
38. E. Yarali, M. Baniasadi, A. Zolfagharian, M. Chavoshi, F. Arefi, M. Hossain, A. Bastola, M. Ansari, A. Foyouzat, A. Dabbagh, M. Ebrahimi, M. J. Mirzaali, M. Bodaghi, Magneto-/electro-responsive polymers toward manufacturing, characterization, and biomedical/soft robotic applications. *Appl. Mater. Today* **26**, 101306 (2022).
39. Y. Itoh, D. Morishita, Development of electroresponsive functional soft materials by electroresponsive dopants. *Polym. J.* **55**, 1035–1048 (2023).
40. A. Lendlein, O. E. C. Gould, Reprogrammable recovery and actuation behaviour of shape-memory polymers. *Nat. Rev. Mater.* **4**, 116–133 (2019).
41. J. Huang, Y. Jiang, Q. Chen, H. Xie, S. Zhou, Bioinspired thermadapt shape-memory polymer with light-induced reversible fluorescence for rewritable 2D/3D-encoding information carriers. *Nat. Commun.* **14**, 7131 (2023).
42. M. A. González-González, A. Kanneganti, A. Joshi-Imre, A. G. Hernandez-Reynoso, G. Bendale, R. Modi, M. Ecker, A. Khurram, S. F. Cogan, W. E. Voit, M. I. Romero-Ortega, Thin film multi-electrode softening cuffs for selective neuromodulation. *Sci. Rep.* **8**, 16390 (2018).
43. Y. Jiao, Y. Zhang, H. Feng, H. Li, Z. Wang, P. Wang, Y. Wang, N. Zheng, T. Xie, Y. Ma, X. Feng, A multifunctional bioelectronic device with switchable rigidity and reconfigurable shapes for comprehensive diagnosis. *Adv. Electron. Mater.* **9**, 2201343 (2023).
44. A. Kotikian, R. L. Truby, J. W. Boley, T. J. White, J. A. Lewis, 3D printing of liquid crystal elastomeric actuators with spatially programed nematic order. *Adv. Mater.* **30**, 1706164 (2018).
45. T. Ware, D. Simon, D. E. Arreaga-Salas, J. Reeder, R. Rennaker, E. W. Keefer, W. Voit, Fabrication of responsive, softening neural interfaces. *Adv. Funct. Mater.* **22**, 3470–3479 (2012).
46. M. D. Dickey, Stretchable and soft electronics using liquid metals. *Adv. Mater.* **29**, 1606425 (2017).
47. M. Zhang, X. Chen, Y. Sun, M. Gan, M. Liu, S.-Y. Tang, S. Zhang, X. Li, W. Li, L. Sun, A magnetically and thermally controlled liquid metal variable stiffness material. *Adv. Eng. Mater.* **25**, 2201296 (2023).
48. D. Hwang, E. J. Barron III, A. B. M. T. Haque, M. D. Bartlett, Shape morphing mechanical metamaterials through reversible plasticity. *Sci. Robot.* **7**, eabg2171 (2022).
49. S. Nam, G. D. Cha, S.-H. Sunwoo, J. H. Jeong, H. Kang, O. K. Park, K.-Y. Lee, S. Oh, T. Hyeon, S. H. Choi, S.-P. Lee, D.-H. Kim, Needle-like multifunctional biphasic microfiber for minimally invasive implantable bioelectronics. *Adv. Mater.* **36**, 2404101 (2024).
50. Y. Lin, J. Genzer, M. D. Dickey, Attributes, fabrication, and applications of gallium-based liquid metal particles. *Adv. Sci.* **7**, 2000192 (2020).
51. K. Y. Kwon, V. K. Truong, F. Krisnadi, S. Im, J. Ma, N. Mehrabian, T. Kim, M. D. Dickey, Surface modification of gallium-based liquid metals: Mechanisms and applications in biomedical sensors and soft actuators. *Adv. Intell. Syst.* **3**, 2000159 (2021).
52. R. Xing, J. Yang, D. Zhang, W. Gong, T. V. Neumann, M. Wang, R. Huang, J. Kong, W. Qi, M. D. Dickey, Metallic gels for conductive 3D and 4D printing. *Matter* **6**, 2248–2262 (2023).
53. J. Suikkola, T. Björninen, M. Mosallaei, T. Kankkunen, P. Iso-Ketola, L. Ukkonen, J. Vanhala, M. Mäntysalo, Screen-printing fabrication and characterization of stretchable electronics. *Sci. Rep.* **6**, 25784 (2016).
54. W. Li, S. Yang, A. Shamim, Screen printing of silver nanowires: Balancing conductivity with transparency while maintaining flexibility and stretchability. *npj Flex. Electron.* **3**, 13 (2019).
55. X. Tang, X. Yan, Dip-coating for fibrous materials: Mechanism, methods and applications. *J. Sol-Gel Sci. Technol.* **81**, 378–404 (2017).
56. Y. Deguchi, M. Kono, Y. Koizumi, Y. Watanabe, M. Fujita, Y. Izato, A. Miyake, Study on autocatalytic decomposition of dimethyl sulfoxide (DMSO) III: Investigations regarding the main decomposition. *Org. Process Res. Dev.* **25**, 2669–2678 (2021).
57. S. Lee, S. A. Jaseem, N. Atar, M. Wang, J. Y. Kim, M. Zare, S. Kim, M. D. Bartlett, J.-W. Jeong, M. D. Dickey, Connecting the dots: Sintering of liquid metal particles for soft and stretchable conductors. *Chem. Rev.* **125**, 3551–3585 (2025).
58. S. Liu, S. N. Reed, M. J. Higgins, M. S. Titus, R. Kramer-Bottiglio, Oxide rupture-induced conductivity in liquid metal nanoparticles by laser and thermal sintering. *Nanoscale* **11**, 17615–17629 (2019).
59. S. Zheng, X. Wang, W. Li, Z. Liu, Q. Li, F. Yan, Pressure-stamped stretchable electronics using a nanofibre membrane containing semi-embedded liquid metal particles. *Nat. Electron.* **7**, 576–585 (2024).
60. L. Tang, L. Mou, W. Zhang, X. Jiang, Large-scale fabrication of highly elastic conductors on a broad range of surfaces. *ACS Appl. Mater. Interfaces* **11**, 7138–7147 (2019).
61. H. Wang, Y. Yao, Z. He, W. Rao, L. Hu, S. Chen, J. Lin, J. Gao, P. Zhang, X. Sun, X. Wang, Y. Cui, Q. Wang, S. Dong, G. Chen, J. Liu, A highly stretchable liquid metal polymer as reversible transitional insulator and conductor. *Adv. Mater.* **31**, e1901337 (2019).
62. S. Jiang, D. C. Patel, J. Kim, S. Yang, W. A. Mills III, Y. Zhang, K. Wang, Z. Feng, S. Vijayan, W. Cai, A. Wang, Y. Guo, I. F. Kimbrough, H. Sontheimer, X. Jia, Spatially expandable fiber-based probes as a multifunctional deep brain interface. *Nat. Commun.* **11**, 6115 (2020).
63. X. Ren, W. Bai, S. Chen, Y. Yuan, X. Shao, X. Zhu, L. Wang, Q. Jiang, B. Hu, Uniaxial extending neural probes for bleeding-absent implantation. *npj Flex. Electron.* **8**, 36 (2024).
64. Y. Tian, C. Zhou, K. Zhang, H. Yang, Z. Chen, Y. Ye, Z. Zhou, X. Wei, T. H. Tao, L. Sun, Self-stretchable Christmas-tree-shaped ultraflexible neural probes. *IEEJ Trans. Elec. Electron. Eng.* **19**, 814–818 (2024).
65. C. Lu, S. Park, T. J. Richner, A. Derry, I. Brown, C. Hou, S. Rao, J. Kang, C. T. Moritz, Y. Fink, P. Anikeeva, Flexible and stretchable nanowire-coated fibers for optoelectronic probing of spinal cord circuits. *Sci. Adv.* **3**, e1600955 (2017).
66. Y. Kim, Y. Lee, J. Yoo, K. S. Nam, W. Jeon, S. Lee, S. Park, Multifunctional and flexible neural probe with thermally drawn fibers for bidirectional synaptic probing in the brain. *ACS Nano* **18**, 13277–13285 (2024).
67. K. Deisseroth, Optogenetics. *Nat. Methods* **8**, 26–29 (2011).
68. L. A. Gunaydin, O. Yizhar, A. Berndt, V. S. Sohal, K. Deisseroth, P. Hegemann, Ultrafast optogenetic control. *Nat. Neurosci.* **13**, 387–392 (2010).

Acknowledgments

Funding: This work was supported by the National Research Foundation of Korea [RS-2024-00335066, RS-2022-NR070824, and RS-2022-NR068144 (J.-W.J.); RS-2024-00420452 (Steve Park); and RS-2023-KI002692], the Boston-Korea Project [RS-2024-00467213 (Seongjun Park)], and the BK21 FOUR (Connected AI Education & Research Program for Industry and Society Innovation, KAIST EE; no. 4120200113769). **Author contributions:** Writing—original draft: S.L., J.-W.J., G.-H.L., and Seongjun Park. Conceptualization: S.L., J.-W.J., M.D.D., G.-H.L., Seongjun Park, and Steve Park. Investigation: S.L., G.-H.L., S.K., Seongjun Park, Y.A., Steve Park, and I.K. Writing—review and editing: S.L., J.-W.J., W.J., M.D.D., G.-H.L., Seongjun Park, D.A.K., Steve Park, and C.Y.K. Methodology: S.L., J.-W.J., W.J., G.-H.L., Seongjun Park, Steve Park, and I.K. Data curation: S.L., W.J., G.-H.L., Y.A., and Steve Park. Validation: S.L., G.-H.L., Steve Park, and I.K. Resources: J.-W.J., M.D.D., G.-H.L., Seongjun Park, Y.A., and Steve Park. Funding acquisition: J.-W.J. and Seongjun Park. Supervision: S.L., J.-W.J., M.D.D., Seongjun Park, and Steve Park. Formal analysis: S.L., G.-H.L., Steve Park, and I.K. Software: S.L., G.-H.L., and I.K. Project administration: S.L., J.-W.J., M.D.D., Seongjun Park, and Steve Park. Visualization: S.L., J.-W.J., G.-H.L., Steve Park, I.K., and Y.A. **Competing interests:** The authors declare that they have no competing interests. **Data and materials availability:** All data needed to evaluate the conclusions in the paper are present in the paper and/or the Supplementary Materials.

Submitted 20 December 2024
Accepted 25 April 2025
Published 30 May 2025
10.1126/sciadv.adv4921